



- 1 **Field assessments on impact of CO₂ concentration fluctuations along with complex**
- 2 **terrain flows on the estimation of the net ecosystem exchange of temperate forests**
- 3 Dexiong Teng^{1,2}, Jiaojun Zhu^{1,2,3,*}, Tian Gao^{1,2,3}, Fengyuan Yu^{1,2}, Yuan Zhu^{1,2}, Xinhua
- 4 Zhou^{3,4}, Bai Yang⁴
- 5 1 Institute of Applied Ecology, Chinese Academy of Sciences, Shenyang 110000, China
- 6 2 Qingyuan Forest CERN, National Observation and Research Station, Liaoning Province,
- 7 Shenyang 110016, China
- 8 3 CAS-CSI Joint Laboratory of Research and Development for Monitoring Forest Fluxes of Trace
- 9 Gases and Isotope Elements, Institute of Applied Ecology, Chinese Academy of Sciences,
- 10 Shenyang 110016, China
- 11 4 Campbell Scientific Incorporation, Logan, Utah 84321, USA
- 12 *** Corresponding Author: Jiaojun Zhu**
- 13 Tel : +86 24 83970342
- 14 Email: jiaojunzhu@iae.ac.cn



15 **Abstract**

16 The CO₂ storage (F_s) is the cumulation or depletion in CO₂ amount over a period
17 in an ecosystem. Along with the eddy-covariance flux and wind-stream advection of
18 CO₂, it is a major term in the net ecosystem CO₂ exchange (NEE) equation and even
19 dominates in the equation under a stable atmospheric stratification while this equation
20 is used for forest ecosystems over complex terrains. However, estimating the F_s remains
21 challenging due to the frequent gusts and random fluctuations in boundary-layer flows
22 that arouse tremendous difficulties in catching the true trend of CO₂ changes for its
23 storage estimation from eddy-covariance along with the atmospheric profile techniques.
24 Using the measurements from Qingyuan Ker Towers equipped with NEE instrument
25 systems separately covering mixed-broadleaf, oak, and larch forests towers in a
26 mountain watershed, this study investigates the gust periods and CO₂ fluctuation
27 magnitudes while examining their impact on F_s estimation in relation to the terrain
28 complexity index (TCI). The gusts induce CO₂ fluctuations at numerous periods of 1 to
29 10 min over two hours. Diurnal, seasonal, and spatial differences ($P < 0.01$) in the
30 maximum amplitude of CO₂ fluctuations (A_{\max}) ranges from 1.6 to 136.7 ppm and these
31 difference in a period (P_{\max}) at the same significant level ranges 140 to 170 second. The
32 A_{\max} and P_{\max} are significantly correlated to the magnitude and random error of F_s with
33 diurnal and seasonal differences. These correlations decrease as CO₂ averaging time
34 windows becomes longer. To minimize the uncertainties of F_s , a constant [CO₂]
35 averaging time window for the F_s estimates is not ideal. Dynamic averaging time
36 windows and a decision-level fusion model can reduce the potential underestimation of



37 F_s by 29%–33%, being equivalent to 1.9%–4.3% underestimation of the NEE for
38 temperate forests in complex terrains. The relative contribution of F_s to the 30-min NEE
39 observations ranged from 17% to 82% depending on wind speed and TCI. The study's
40 approach is notable as it incorporates TCI and utilizes three flux towers for replication,
41 making the findings relevant to similar regions with a single tower.

42 **Keywords:** Eddy covariance, complex terrain, carbon flux, storage term, carbon
43 dioxide concentration, random uncertainty

44 1 Introduction

45 The accurate estimation of the net ecosystem exchange (NEE) of carbon dioxide
46 (CO_2) in forest ecosystems is crucial for a comprehensive understanding of the global
47 carbon cycle. The eddy covariance (EC) technique has been widely used in forest
48 ecosystems due to its capacity to directly measure the NEE while measurement
49 conditions satisfy the underlying theory. The EC technique is based on a simplified
50 mass conservation equation (after the Reynolds averaging), given by:

$$\begin{aligned} \text{NEE} = & \underbrace{\frac{1}{V_m} \int_0^h \left(\frac{\partial \bar{c}}{\partial t} \right) dz}_{\text{I}} + \underbrace{\frac{1}{V_m} (\overline{w'c'})_h}_{\text{II}} \\ & + \underbrace{\frac{1}{V_m} \int_0^h \left(\bar{w}(z) \frac{\partial \bar{c}}{\partial z} + \bar{c}(z) \frac{\partial \bar{w}}{\partial z} \right) dz}_{\text{III a}} + \underbrace{\frac{1}{V_m} \int_0^h \left(\bar{u}(z) \frac{\partial \bar{c}}{\partial x} + \bar{v}(z) \frac{\partial \bar{c}}{\partial y} \right) dz}_{\text{IV}}, \end{aligned} \quad (1)$$

52 where V_m is the volume of dry air in the control volume; c is the CO_2 mixing ratio; t is
53 the time; h is the measure height; u , v , and w denote the velocity components in the x ,



54 y , and z directions, respectively; and an overbar denotes Reynolds averaging. This
55 equation conceptualizes the NEE within a control volume from the ground to the
56 measurement height (h), while ignoring the horizontal turbulence term divergence
57 (Feigenwinter et al., 2004). In this equation, term I is the CO₂ storage (F_s) representing
58 the change in the average CO₂ concentration (hereafter [CO₂]). Terms II, IIIa, IIIb, and
59 IV represent the vertical turbulent flux (F_c), the vertical advection, the interface vertical
60 mass advection, such as the evaporation process (Webb et al., 1980), and the horizontal
61 advection, respectively.

62 Most flux measurements typically lack the solutions for terms III and IV, and can
63 only estimate the NEE by summing F_c and F_s , and even a significant number of sites
64 ignored the F_s . The F_s in the vertical gas column within a canopy can be substantial,
65 requiring attention in NEE estimates (Aubinet et al., 2000). The F_s contributes ~60% to
66 nocturnal turbulent flux underestimation in forest ecosystems with “ideal” topography
67 (Mchugh et al., 2017). Especially, during atmospherically stable periods such as the
68 early morning, sunset, and nighttime transitions, the F_s has a significant impact on the
69 NEE. For 30-min and annual forest ecosystem carbon flux measurements, ignoring F_s
70 would underestimate the NEE (Zhang et al., 2010). The F_s value typically ranges from
71 -2 to $-5 \mu\text{mol m}^{-2} \text{s}^{-1}$ in the early morning, and the F_s is about $1-3 \mu\text{mol m}^{-2} \text{s}^{-1}$ after
72 sunset for temperate forests. Neglecting the F_s value can also lead to a misunderstanding
73 of the CO₂ exchange processes, such as ecosystem respiration and photosynthesis, and
74 their relationship with key control factors such as solar radiation, temperature, and
75 moisture (Mchugh et al., 2017). Therefore, it is imperative not to overlook F_s to ensure



76 more precise NEE estimates of forest ecosystems, particularly in complex terrains.

77 Despite the challenges inherent in monitoring forest conditions, understanding the
78 carbon flux of forest ecosystems in complex terrains or with heterogeneous underlying
79 surfaces remains an area of great interest. Topography complexity plays a complex role
80 in the transportation of momentum, energy, and mass in the atmospheric boundary layer,
81 with direct impacts on the airflow patterns, spatiotemporal characteristics, and gas
82 concentration fluctuations (Sha et al., 2021; Finnigan et al., 2020). Differences in
83 airflow along the slope, lateral CO₂ discharge downhill, and spatiotemporal variations
84 in soil respiration result in the CO₂ outflow from slopes and valleys lagging behind the
85 flat top of the mountain (De Araújo et al., 2010). At night, under stable atmospheric
86 stratification, cold air moves from the ground to the valley forest canopy and then flows
87 to low-lying areas, causing a “carbon pooling” effect. The gradient of [CO₂] below the
88 EC sensors fluctuates significantly, and the cold air discharge above the canopy reduces
89 CO₂ storage, leading to an underestimation of forest ecosystem respiration (Yao et al.,
90 2011; De Araújo et al., 2008; De Araújo et al., 2010).

91 According to the theoretical definition, F_s estimates are derived by averaging the
92 [CO₂] of the control volume at the beginning and the end of the EC averaging period
93 (30 min or 1 h) and dividing by the EC averaging period (Finnigan, 2006). In practice,
94 the F_s represents the integration of the time derivative of the vertically determined
95 column-averaged [CO₂]. However, relying solely on tower-top measurements can lead
96 to underestimation of F_s by up to 34% compared to the eight-level profile approach (Gu
97 et al., 2012). The NEE magnitude with the F_s based on the two-min [CO₂] averaging



98 time window (instantaneous concentration approach) was found to be 5% higher than
99 that of the 30-min-window-based F_s (averaging concentration approach), particularly
100 during nighttime in the growing season (Wang et al., 2016). The effect of the F_s on the
101 NEE of forest ecosystems increases with the increase of timescale, and the annual sum
102 of the NEE obtained using the instantaneous concentration approach is higher than that
103 obtained by averaging concentrations (Li et al., 2020). Most research has examined how
104 vertical and horizontal gas concentration sampling point distribution affects the
105 uncertainty in F_s estimation (Bjorkegren et al., 2015; Wang et al., 2016; Yang et al.,
106 2007; Yang et al., 1999), with a small number of studies examining the effect of $[CO_2]$
107 sampling frequency on the F_s (Finnigan, 2006; Heinesch et al., 2007). Certain studies
108 have experimentally validated new concepts, such as correlating the gas sampling point
109 concentration with the horizontal distribution (Nicolini et al., 2018). Some studies have
110 approached the true value theoretically, such as through defining the control volume
111 represented by flux measurements (Metzger, 2018; Xu et al., 2019). However, the
112 number of complete column samples required to describe the column-averaged $[CO_2]$
113 of each 30-min or 1-h F_s estimate is still undetermined.

114 Previous studies have emphasized the significance of the F_s to the NEE and the
115 influence of $[CO_2]$ dynamics on F_s estimates in complex terrains. To overcome any
116 disparities between sensors and obtain precise changes in the $[CO_2]$ gradient above and
117 below the forest canopy, individual gas analyzers are extensively utilized to measure
118 $[CO_2]$ levels vertically (Siebicke et al., 2011). However, a single gas analyzer introduces
119 time delays when monitoring multi-point $[CO_2]$ curves. Accurately determining the F_s



120 estimates can be challenging due to the spatial and temporal resolution of [CO₂]
121 measurements (Wang et al., 2016). The random error of the F_s estimates using one
122 complete column sample is considerably high due to short-term [CO₂] fluctuations
123 (Nicolini et al., 2018). The calculation of the F_s using time-averaged [CO₂] profiling
124 leads to significant information loss at high frequency, resulting in a substantial
125 underestimation bias. Furthermore, resource constraints in the measurement system,
126 coupled with a lack of clear guidelines for estimating the F_s values and their associated
127 uncertainties, create a significant gap between ideal initiatives and their implementation.
128 These issues necessitate further efforts to characterize [CO₂] fluctuations across
129 different sites and demonstrate the mechanisms influencing F_s magnitudes,
130 uncertainties, and their contributions to NEE observations in complex terrains. Thus,
131 this manuscript aims to bridge this gap by introducing a statistical method to estimate
132 F_s values and their uncertainties.

133 This paper employed an innovative EC site with three flux towers (Qingyuan-Ker
134 Towers) to monitor three typical types of temperate forest stands located in complex
135 terrains in northeastern China. This study introduces a decision-level fusion model
136 based on weighing the underestimation bias and random error of the F_s to obtain more
137 accurate results. The objectives of this study were to: 1) compare diurnal, seasonal, and
138 spatial differences in [CO₂] fluctuations, F_s, and its uncertainty; 2) examine the
139 variation in F_s uncertainty with different [CO₂] averaging time windows; and 3)
140 investigate the response of F_s and its uncertainty to [CO₂] fluctuations, wind above the
141 canopy, and terrain complexity, and quantify the impact of the F_s on the NEE estimates

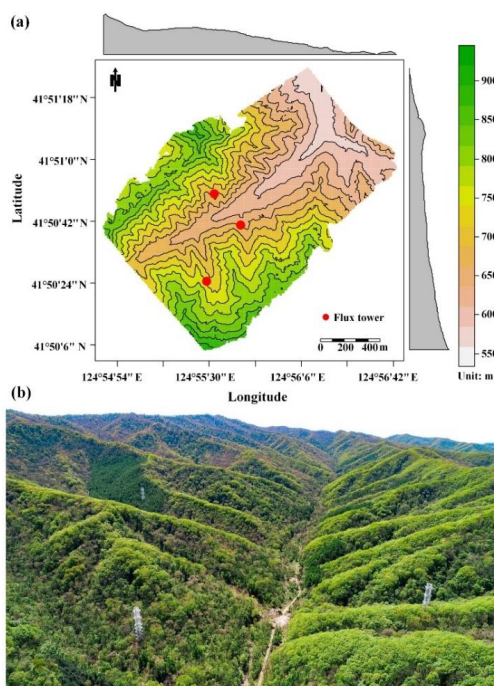


142 under these conditions.

143 2 Materials and methods

144 2.1 Study site and instrumental set-up

145 This study was conducted in temperate forests in a watershed based on the Ker
146 towers (Zhu et al., 2021; Gao et al., 2020), situated in northeast China ($41^{\circ}50'N$,
147 $124^{\circ}56'E$). The region experiences a temperate continental monsoon climate, with an
148 average annual temperature of $4.3^{\circ}C$ and annual rainfall of 758 mm from 2010 to 2021
149 (Li et al., 2023). The Ker towers consist of three 50-m-high EC towers (Fig. 1) that
150 observe a mixed broadleaved forest (MBF), a Mongolian oak forest (MOF), and a Larch
151 plantation forest (LPF).



152

153 Fig. 1 Overview of the study area. The first map (a) depicts the topography of the study site, with



154 black curves indicating elevation contours, and marginal distributions represented as a gray graph,
 155 averaged over rows and columns. The second image (b) features an aerial photograph of the
 156 Qingyuan-Ker towers captured in the growing season (Gao et al., 2020).

157 The basic information regarding Ker towers in this study is presented in Table 1.

158 The closed-path EC system (EC310, Campbell Scientific Ltd., Logan, UT, USA),
 159 comprising a CSAT3 sonic anemometer and an EC155 closed-path infrared ray gas
 160 analyzer (IRGA), was employed to monitor the three-dimensional wind speed and
 161 CO₂/H₂O concentrations (10 Hz). The atmospheric profiling system (AP200, Campbell
 162 Scientific Ltd., Logan, UT, USA) was utilized to measure the CO₂/H₂O concentrations
 163 with eight height levels. Each level was measured for 15 s (with 10 s for the flushing
 164 of the manifold and 5 s for logging the average), leading to a measurement cycle of 2
 165 min.

166 Table 1 Basic information of Ker towers

Forest	Mixed broad-leaved	Mongolian oak	Larch plantation
Experiment period	Jan 01, 2020– Dec 31, 2021	Jan 01, 2020– Dec 31, 2021	Jan 01, 2020– Dec 31, 2021
Elevation (m)	634	669	721
Slope (°)	14.8 ± 2.1	19.1 ± 2.9	16.2 ± 5.3
Canopy height (m)	21.5 ± 1.8	13.9 ± 0.6	19.5 ± 0.6
Leaf area indices	3.0 ± 0.5	3.1 ± 0.8	3.9 ± 0.6
Eddy covariance system	EC310	EC310	EC310
Eddy covariance sensor height (m)	46	46	36
Atmospheric profiling system	AP200	AP200	AP200
Profile heights (m)	0.5, 2, 6, 11, 16, 21, 26, 36	0.5, 2, 6, 11, 16, 21, 26, 36	0.5, 2, 6, 11, 16, 21, 26, 36



167 2.2 Calculation of storage flux

168 Averaging the $[\text{CO}_2]$ in a time window was utilized to calculate the F_s values, in
169 addition to data on the air pressure, $\text{CO}_2/\text{H}_2\text{O}$ molar fractions, and air temperature at
170 different heights above the ground surface (Finnigan, 2006; Montagnani et al., 2018;
171 Xu et al., 2019). The molar mixing ratio and mass mixing ratio are conserved quantities
172 with the variation of air temperature, air pressure, and water vapor concentration,
173 whereas the molar fraction is not. This study determined the F_s using the molar mixing
174 ratio obtained from $\text{CO}_2/\text{H}_2\text{O}$ molar fraction observations, applying the ideal gas law
175 and Dalton's partial pressure law (Montagnani et al., 2009). The water vapor molar
176 mixing ratio (χ_v) in mmol mol^{-1} is given by

$$\chi_v = \frac{c_v}{1 - c_v \times 10^{-3}}, \quad (2)$$

177 where c_v is the water vapor molar fraction in mmol mol^{-1} , and the CO_2 molar mixing
178 ratio (χ_c) in $\mu\text{mol mol}^{-1}$ is given by

$$\chi_c = \frac{c_c}{1 - c_v \times 10^{-3}}, \quad (3)$$

179 where c_c is the CO_2 molar fraction in $\mu\text{mol mol}^{-1}$.

180 The dry air density ($\bar{\rho}_d$) in mol m^{-3} is calculated as follows:

$$\bar{\rho}_d = \frac{\bar{P}}{(\bar{T} + 273.15) \times (R^* + \chi_v \times 10^{-3} \cdot R^* \cdot M_d/M_v)}, \quad (4)$$

181 where R^* is the air gas constant ($8.31441 \text{ Pa m}^3 \text{ K}^{-1} \text{ mol}^{-1}$), \bar{P} is the air pressure in
182 Pa, and \bar{T} is the average air temperature in Celsius. M_d and M_v are the dry air and
183 water vapor molar mass ($18.015 \text{ g mol}^{-1}$), respectively. M_d is calculated from the CO_2
184 molar mixing ratio (Khélifa et al., 2007):



$$M_d = 28.9635 + M_c \cdot (\chi_c \times 10^{-6} - 0.0004), \quad (5)$$

185 where M_c is the CO₂ molar mass (12.011 g mol⁻¹).

186 The F_s estimated from eight-level profiles are calculated as follows:

$$F_s = \bar{\rho}_d \int_0^h \frac{d\bar{\chi}_c}{dt} dz \doteq \bar{\rho}_d \sum_{i=1}^8 \frac{\Delta\bar{\chi}_{c_i} \Delta h_i}{\Delta t}, \quad (6)$$

187 where $\bar{\chi}_c$ is the average CO₂ molar mixing ratio and Δh_i is the height represented by
188 each level. To ensure that F_s corresponds to F_c in time, the average [CO₂] at the start or
189 end moments (t) during a time window (τ min) is calculated as follows:

$$\bar{\chi}_{c_i} = \frac{2}{\tau} \sum_{t-\frac{\tau}{2} < t \leq t+\frac{\tau}{2}} \chi_{c_i}(t). \quad (7)$$

190 2.3 Data analysis

191 To evaluate the impact of [CO₂] fluctuations on F_s measurements and its
192 corresponding uncertainty, empirical modal decomposition (EMD) and Fourier
193 spectrum analysis were used to extract the period and amplitude of fluctuations in the
194 high-frequency [CO₂] time series (10 Hz). EMD was used to decompose the [CO₂] time
195 series into intrinsic mode functions based on local signal properties, which yield
196 instantaneous frequencies as functions of time, allowing for the identification of
197 embedded structures of eddies. EMD is applicable to non-linear and non-stationary
198 processes (Huang et al., 1998). The period and amplitude of [CO₂] fluctuations above
199 the forest canopies reflected the eddy size. Subsequently, the maximum period and
200 amplitude of [CO₂] fluctuations in a short term (2h) was indicative of large eddies under
201 the influence of gust.

202 Due to the diurnal and seasonal variability of flux measurements, this study



203 defined the transition period and growing season. The solar elevation angle was used
204 to define the transition period as 1-h before sunrise (sunset) to 2-h after sunrise (sunset).
205 The growing degree days (GDDs) were calculated using the base temperature (T_{base}) to
206 determine the beginning and end of the growing season, and the formula was as follows
207 (Mcmaster and Wilhelm, 1997):

$$GDD = \frac{1}{2}(T_{max} + T_{min}) - T_{base}, \quad (8)$$

208 where T_{base} is 6°C . Considering the persistent demand of temperature to support
209 vegetation growth, the fourth day of the first GDD greater than zero (less than zero)
210 over a span of five consecutive days was defined as the starting (ending) time of the
211 growing season.

212 The main data processing and analysis steps are outlined below:

213 1. EMD and Fourier spectrum analysis of $[\text{CO}_2]$ high-frequency time series were
214 used to extract the maximum amplitude (A_{max}) and corresponding period (P_{max}) of $[\text{CO}_2]$
215 fluctuations every 2 h. The data were divided into two subsets based on P_{max} , with a
216 cut-off of 150 s.

217 2. CO_2 storage fluxes were calculated for different $[\text{CO}_2]$ average time windows
218 (τ), ranging from 4 to 28 min.

219 3. The standardized major axis (SMA) regression model (Warton et al., 2012) was
220 used to compare the slope differences (bias) between $F_{s_ \tau}$ and $F_{s_ 28}$ for different P_{max}
221 and the forest stands. The SMA model offers routines for comparing parameters a and
222 b among groups for symmetric problems.

223 4. The normalized root mean square error (NRMSE) and slope were used to



224 evaluate the relative error and bias between F_{s_τ} and $F_{s_{28}}$. The NRMSE is calculated as
225 follows:

$$NRMSE = 100 \times \frac{\sqrt{\sum_{i=1}^N (F_{s_\tau}^{(i)} - F_{s_{28}}^{(i)})^2}}{\sqrt{\sum_{i=1}^N (F_{s_{28}}^{(i)} - \overline{F_{s_{28}}})^2}} \quad (9)$$

226 5. The normalized weighting coefficient (w) of F_{s_τ} was estimated based on the
227 NRMSE and slope (Wang et al., 2020). The details are shown in Appendix A1. Then,
228 using the decision-level fusion model, F_{s_comb} was calculated as follows:

$$F_{s_comb} = w_1^* \cdot F_{s_4} + w_2^* \cdot F_{s_8} + \dots + w_7^* \cdot F_{s_{28}} \quad (10)$$

229 The decision-level fusion model automatically assigned weights to the F_s based on
230 different $[\text{CO}_2]$ averaging time windows. Its purpose in this study was to balance the
231 relative error and bias of F_s estimates caused by $[\text{CO}_2]$ sampling. The analysis was
232 performed using the EMD and smatr R packages (Warton et al., 2012; Huang et al.,
233 1998).

234 2.4 Uncertainty analysis

235 To improve the accuracy of estimating the uncertainty of F_s using individual tower,
236 this work has made modifications to the 24-h difference method by extending the
237 sampling time windows and applying meteorological condition constraints (Hollinger
238 and Richardson, 2005). This method trades time for space to estimate the uncertainty
239 of F_s . To determine the uncertainty of F_s , this study compared the observations at
240 moment i to the average of several observations during a similar period and with similar
241 meteorological conditions. The specific steps were as follows:

242 1. The average F_s was calculated in a certain time window (15 d) for the moment



243 interval ($i-0.5$ h, $i+0.5$ h) where moment i was located and where the meteorological
244 conditions (such as the u^* , air temperature, and sensible heat flux) were similar.

245 2. The difference between the F_s value corresponding to each moment i and $\overline{F_s}$
246 was calculated separately to obtain the residual sequence ε_s .

247 3. The standard deviation $\sigma(\varepsilon_s)$ related to ε_s for F_s was calculated in a certain
248 time window (15 d) for the moment interval ($i-0.5$ h, $i+0.5$ h) where moment i is located
249 and where the meteorological conditions (such as the u^* , air temperature, and sensible
250 heat flux) were similar.

251 After estimating the uncertainty of F_s , this study extended the work conducted by
252 Richardson et al. (2008) to analyze its relationship with the magnitude of flux
253 measurements ($|F_s|$), $[CO_2]$ fluctuations (A_{\max} and P_{\max}), wind speed (WS), and terrain
254 complexity index (TCI). A comprehensible description of the TCI can be found in
255 Appendix A2. This relationship can be approximated by using the following equation:

$$\sigma(\varepsilon_s) = \beta_0 + \sum_{i=1} \beta_i \cdot x_i, \quad (11)$$

256 where the nonzero intercept term β_0 indicates the size of the random uncertainty as
257 x_i approaches 0, which varies with the observation site, with larger value of β_0
258 indicating greater uncertainty. The slope term β_i indicates the sensitivity of the size of
259 the random uncertainty of x_i , with smaller β_i values indicating a probability
260 distribution of uncertainty closer to white noise.



261 **3 Results**

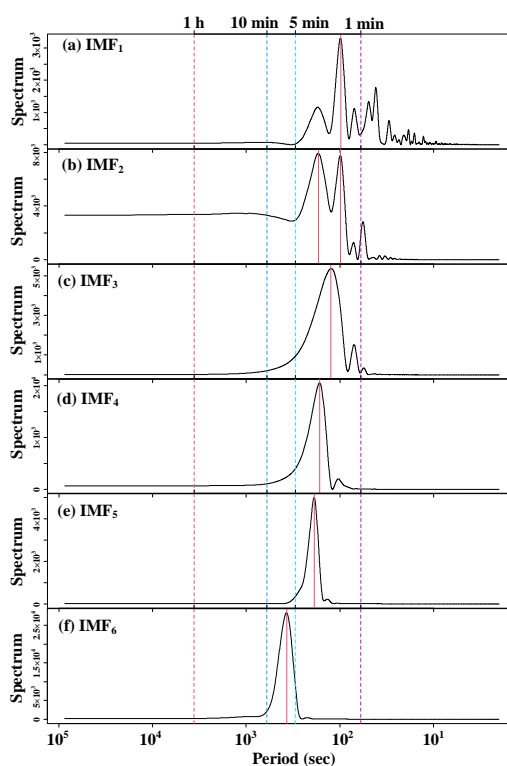
262 3.1 Characterization of [CO₂] fluctuation and F_s variations

263 The [CO₂] high-frequency time series above the forest canopies were decomposed
264 using EMD, followed by spectral analysis to extract the fluctuation period and
265 amplitude of [CO₂] at different time scales. As depicted in Fig. 2, it became evident that
266 the [CO₂] above the canopies displayed short-term fluctuations with periods ranging
267 from 1 to 10 min, and the amplitude of these fluctuations showed an increasing trend
268 with longer periods. This observation strongly suggested the presence of large eddies
269 influenced by gusts above the canopies, and these eddies were responsible for the
270 increasing amplitude of [CO₂] fluctuations as their size increased.

271 To examine the spatio-temporal variations in large eddies, this study compared the
272 A_{\max} and P_{\max} values above canopies across different forest stands. The analysis utilized
273 data from daytime, nighttime, and transition periods in both the growing and dormant
274 seasons. The averages of A_{\max} and P_{\max} averages for the above-canopy [CO₂] in the
275 three forest stands ranged from 1.588 to 136.667 ppm and from 2.313 to 2.784 min,
276 respectively (Table 2). Fig. 3 demonstrated significant seasonal and diurnal differences
277 ($P < 0.01$) in P_{\max} , with higher values during daytime in the growing season, and lower
278 values during the daytime in the dormant season. Moreover, P_{\max} was significantly
279 different ($P < 0.01$) among different forest stands during the same time period, with
280 MBF stand having the highest values, followed by the MOF, and the lowest values in
281 the LPF. During the growing season, the A_{\max} values were significantly higher than



282 those during the dormant season, with both daytime and nighttime values also
 283 exhibiting significant differences ($P < 0.01$) among different forest stands. This
 284 observation provided evidence of significant spatio-temporal variability in large eddies
 285 influenced by gusts.



286
 287 Fig. 2 Power spectral density of the intrinsic mode function (IMF) of above-canopy CO₂
 288 concentrations in the Mongolian oak forest on July 2, 2020 (24 h).

289 Table 2 Mean of the A_{\max} and P_{\max} in different forest stands at different periods

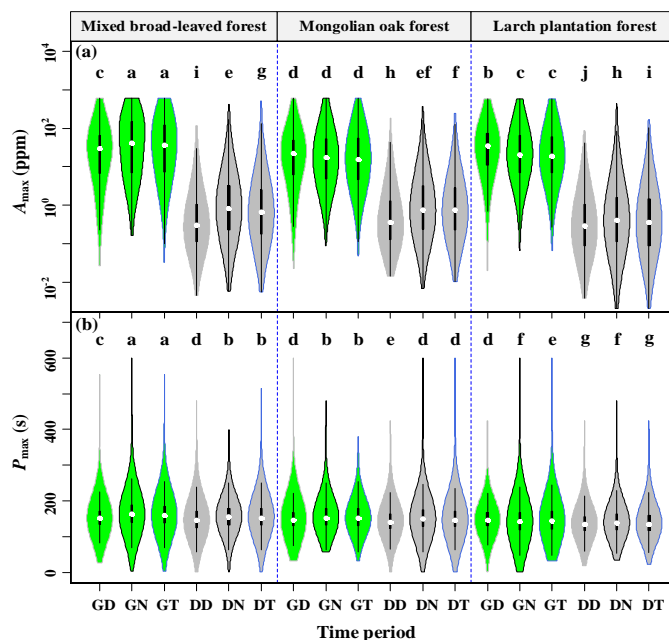
Variable	Tower site	Growing season			Dormant season		
		DT ¹	NT ²	TP ³	DT	NT	TP
A_{\max} ⁴ (ppm)	MBF ⁶	57.932	139.667	136.717	2.219	5.212	4.944
	MOF ⁷	36.160	57.945	55.777	2.699	5.175	4.637
	LPF ⁸	52.688	58.816	60.147	1.588	2.985	2.456
P_{\max} ⁵	MBF	154.563	167.024	164.824	158.449	151.428	158.121



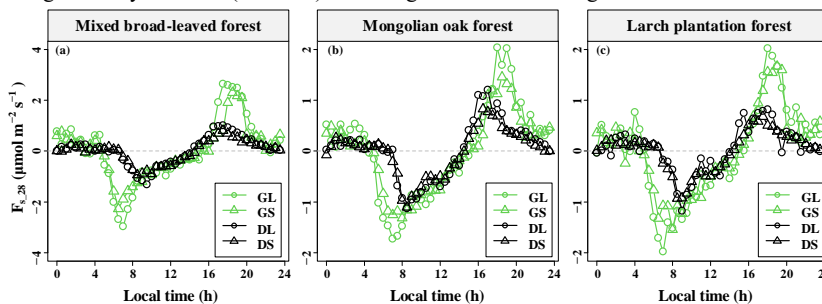
(s)	MOF	151.986	160.633	159.146	153.091	147.491	153.274
	LPF	149.003	143.950	145.696	143.458	138.794	142.009

290 ¹ DT represents daytime; ² NT represents nighttime; ³ TP represents transition period. ⁴ A_{\max}
291 represents the maximum amplitude of short-term CO₂ concentration fluctuations; ⁵ P_{\max} represents
292 the corresponding period of maximum amplitude. ⁶ MBF represents mixed broad-leaved forest; ⁷
293 MOF represents Mongolian oak forest; ⁸ LPF represents Larch plantation forest.

294 To estimate the uncertainty of F_s using an individual tower, a comprehensive
295 analysis of its diurnal and seasonal dynamics, as well as the functional relationship
296 between F_s and u^* , was necessary. Fig. 4 presented significant diurnal variations and
297 seasonal differences in F_s across the three forest stands. During the growing season, the
298 median diurnal variation of F_s for the three forest stands ranged from -2.960 to 2.647
299 $\mu\text{mol m}^{-2} \text{s}^{-1}$, whereas during the dormant season, it ranged from -1.306 to 1.012 μmol
300 $\text{m}^{-2} \text{s}^{-1}$. Comparing the amplitude of F_s diurnal variation among the three forest stands,
301 MBF exhibited the largest amplitude during the growing season, while the amplitudes
302 of the three forest stands were similar during the dormant season. Notably, it was
303 observed that the amplitudes for longer P_{\max} values were greater than those for shorter
304 P_{\max} values. This observation indicated that the larger the eddies, the greater the
305 amplitude of F_s .



306
 307 Fig. 3 Maximum amplitude (A_{\max}) (a) and corresponding period (P_{\max}) (b) of short-term CO_2
 308 concentration fluctuations in different forest stands for seasonal and diurnal variations, where GD,
 309 GN, GT, DD, DN, and DT denote the growing season daytime, growing season nighttime,
 310 growing season transition period, dormant season daytime, dormant season nighttime, and
 311 dormant season transition period, respectively. Columns with different lowercase letters are
 312 significantly different ($P < 0.05$) according to Fisher's least significant difference test.

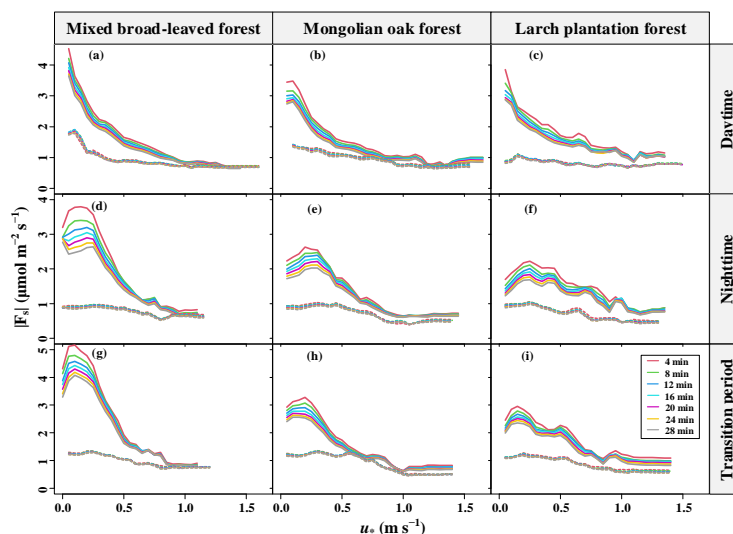


313
 314 Fig. 4 Median diurnal variation of CO_2 storage flux (F_s) based on 28-min CO_2 concentration
 315 averaging time windows in the three forest stands during different seasons. GS indicates the
 316 growing season and a short period of maximum amplitude (P_{\max}), GL indicates the growing
 317 season and a long P_{\max} , DS indicates the dormant season and a short P_{\max} , and DL indicates the
 318 dormant season and a long P_{\max} .

319 Furthermore, a u^* threshold value was identified for the variation of F_s with u^*



320 during daytime in both the dormant and growing seasons (Fig. 5). When u^* fell below
 321 the u^* threshold, the magnitude of F_s ($|F_s|$) decreased with increasing u^* . Conversely,
 322 when u^* exceeded the u^* threshold, the $|F_s|$ tended to remain relatively constant. Notably,
 323 a maximum point for the $|F_s|$ was observed when the u^* was less than 0.5 m/s during the
 324 growing season, whereas not during the dormant season. This phenomenon was
 325 particularly evident during the nighttime and transition periods of the growing season,
 326 where $|F_s|$ exhibited an initial increase followed by a subsequent decrease with u^* . These
 327 observations strongly indicated that the effect of the turbulent mixing strength on the
 328 $|F_s|$ over complex terrains was nonlinear and exhibited diurnal and seasonal differences.



329
 330 Fig. 5 Magnitudes of CO₂ storage flux ($|F_s|$) determined with different CO₂ concentration average
 331 time windows as a function of the friction velocity (u^*) and moving block averages from all 30-
 332 min data for the years 2020-2021. Dashed and solid lines donate the dormant and growing
 333 seasons, respectively.

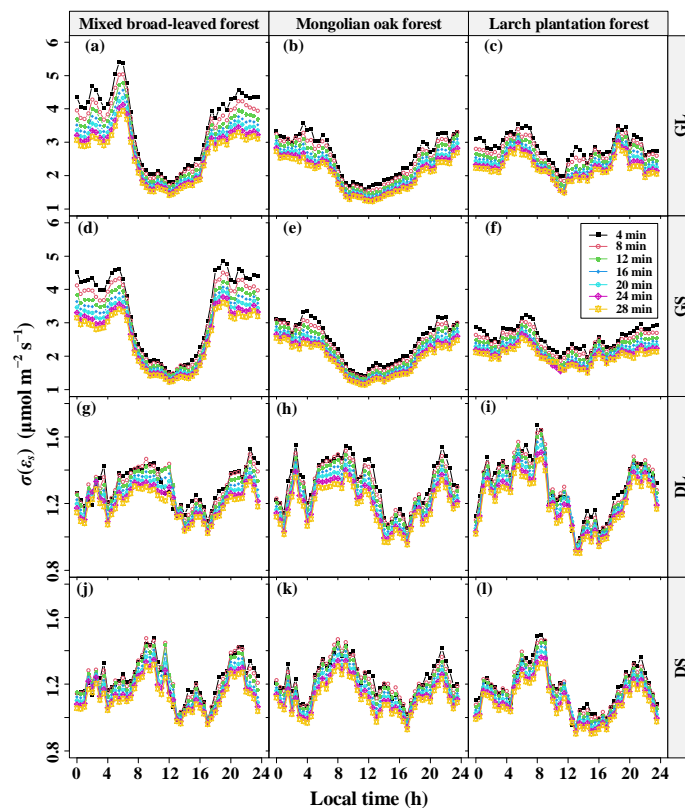
334 3.2 Effect of [CO₂] fluctuations on the F_s and its uncertainty

335 To investigate the influence of the [CO₂] fluctuation periods on the error of F_s



336 measurement, this study computed the diurnal average of the standard deviation $\sigma(\varepsilon_s)$
337 of the 30-min F_s uncertainty (ε_s) separately for different P_{\max} values and the seasons.
338 The overall distribution of ε_s showed a non-normal distribution with a high peak
339 (kurtosis > 2 and $P < 0.05$, results presented in Supplementary Table 1–4). The daily
340 variation curves of $\sigma(\varepsilon_s)$ at various $[\text{CO}_2]$ averaging time windows are presented in
341 Fig. 6. It was observed that the diurnal variation range of $\sigma(\varepsilon_s)$ was higher during the
342 growing season compared to the dormant season, regardless of the P_{\max} lengths,
343 indicating a seasonal difference independent of the P_{\max} . Additionally, during the
344 growing season, both MBF and MOF demonstrated evident diurnal variation in $\sigma(\varepsilon_s)$,
345 with the peak occurring at night and the trough during the daytime. The diurnal
346 variation range of $\sigma(\varepsilon_s)$ varied across the three forest stands, with MBF exhibiting the
347 largest amplitude.

348 Furthermore, a significantly positive correlation was observed between $\sigma(\varepsilon_s)$ the
349 $|F_s|$ ($P < 0.01$), with site, seasonal, and diurnal differences (Fig. 7). The relationship
350 between these variables was characterized by intercepts and slopes that varied across
351 different $[\text{CO}_2]$ averaging time windows, ranging from 1.99 to 2.82 and from 0.24 to
352 0.28, respectively (results presented in the Supplementary Tables 5–6). Both decreased
353 as the $[\text{CO}_2]$ averaging time window increased, with the growing season exhibiting
354 larger values compared to the dormant season (results shown in the Supplementary
355 Tables 5–6). These findings suggested that increasing the $[\text{CO}_2]$ averaging time window,
356 results in a reduction of the random error in F_s , approaching a behavior similar to white
357 noise.

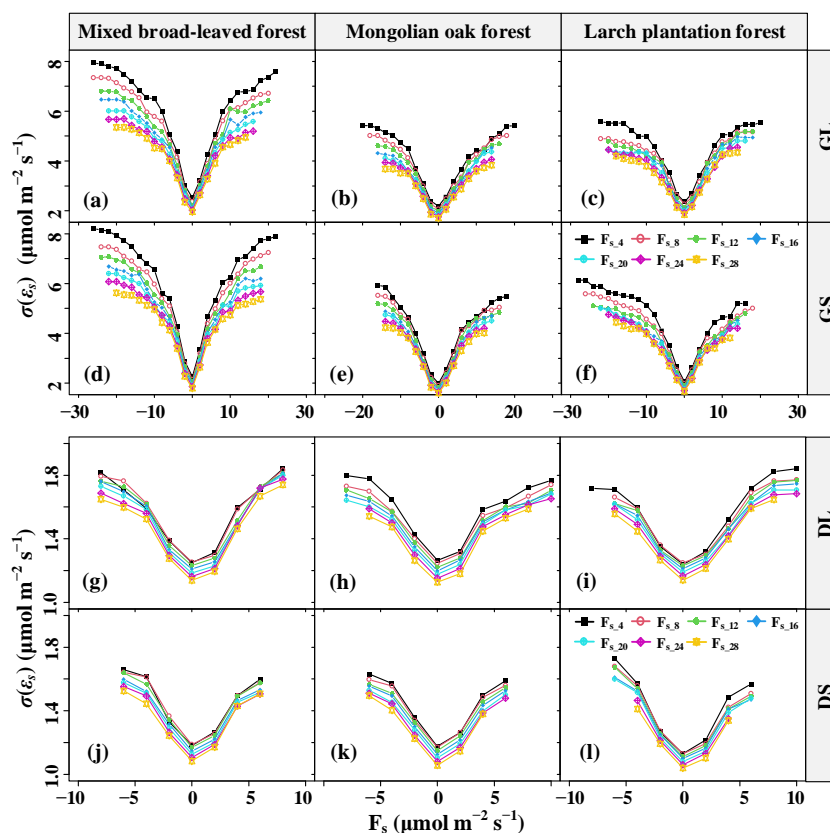


358
 359 Fig. 6 Diurnal variations in the random uncertainty ($\sigma(\epsilon_s)$) of CO_2 storage flux (F_s) errors (ϵ_s) at
 360 different CO_2 concentration ($[\text{CO}_2]$) averaging time windows and their seasonal differences, where
 361 GS indicates the growing season and a short period of maximum amplitude (P_{\max}) of $[\text{CO}_2]$
 362 fluctuations, GL indicates the growing season and a long P_{\max} , DS indicates the dormant season
 363 and a short P_{\max} , and DL indicates the dormant season and a long P_{\max} .

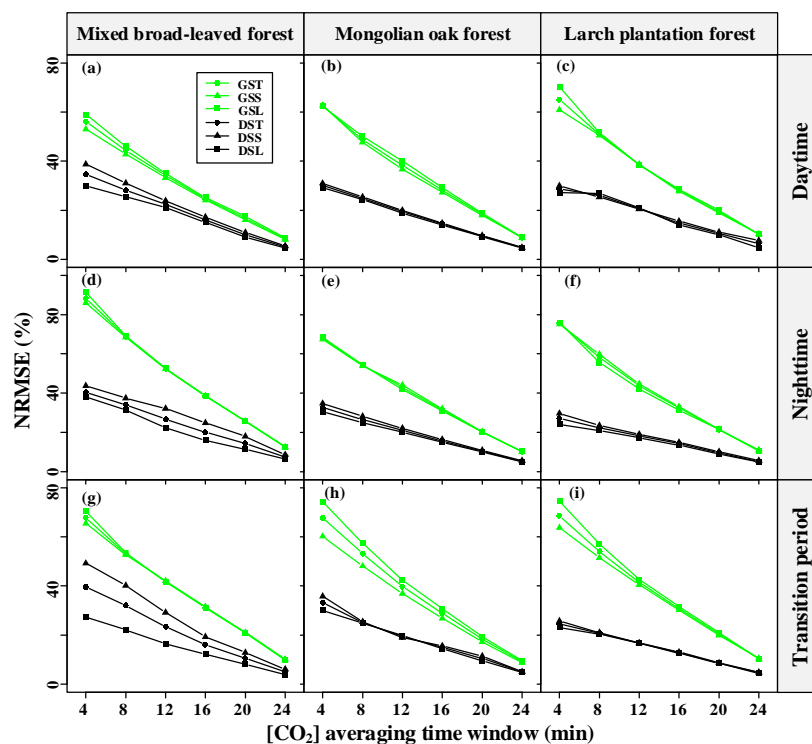
364 To assess the impact of $[\text{CO}_2]$ fluctuations on the error and bias of F_s measurement,
 365 this study compared the NRMSE and slopes of F_s based on different $[\text{CO}_2]$ averaging
 366 time windows, with reference to the baseline F_{s_28} , across various P_{\max} values, time
 367 periods, and sites. As shown in Fig. 8, the NRMSE decreased and approached
 368 convergence as the $[\text{CO}_2]$ averaging time windows increased. During both daytime and
 369 nighttime in the growing season, the NRMSE corresponding to longer P_{\max} was greater
 370 than that corresponding to shorter P_{\max} , while the opposite trend was observed during



371 the dormant season. Additionally, the longer the $[\text{CO}_2]$ averaging time window, the
 372 greater the relative underestimation of F_s .



373
 374 Fig. 7 Random uncertainty $\sigma(\varepsilon_s)$ of CO_2 storage flux (F_s) errors (ε_s) at different CO_2
 375 concentration ($[\text{CO}_2]$) averaging time windows as a function of the F_s magnitude for mixed broad-
 376 leaved forest, Mongolian oak forest, and Larch plantation forest during the growing and dormant
 377 seasons. GS indicates the growing season and a short period of maximum amplitude (P_{max}) of
 378 $[\text{CO}_2]$ fluctuations, GL indicates the growing season and a long P_{max} , DS indicates the dormant
 379 season and a short P_{max} , and DL indicates the dormant season and a long P_{max} .

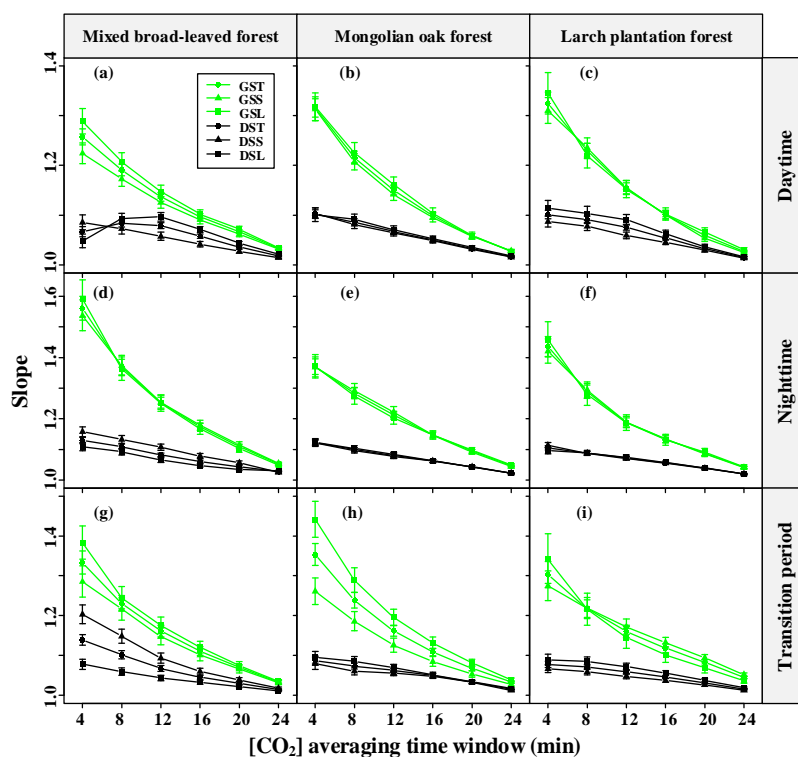


380
 381 Fig. 8 Seasonal and diurnal differences in the normalized root mean square error (NRMSE) of
 382 CO_2 storage flux (F_s) versus the respective F_{s_28} values for different CO_2 concentration ($[\text{CO}_2]$)
 383 averaging time windows. GST indicates the growing season and does not distinguish the period of
 384 maximum amplitude (P_{\max}) of $[\text{CO}_2]$ fluctuations, GSS indicates the growing season and a short
 385 P_{\max} , GSL indicates the growing season and a long P_{\max} , DST indicates the dormant season and
 386 does not distinguish P_{\max} , DSS indicates the dormant season and a short P_{\max} , and DSL indicates
 387 the dormant season and a long P_{\max} .

388 The comparison of slopes between F_{s_4} and F_{s_28} in the three forest stands revealed
 389 interesting patterns, as depicted in Fig. 9. During the growing season, the slopes
 390 corresponding to the shorter P_{\max} of $[\text{CO}_2]$ fluctuations were consistently lower than
 391 those for the longer P_{\max} , indicating that the effect of P_{\max} on F_s uncertainty decreased
 392 with increasing $[\text{CO}_2]$ averaging time windows. However, for the MBF stand (Fig. 9d
 393 and Fig. 9g), the slopes corresponding to the shorter P_{\max} of $[\text{CO}_2]$ fluctuations during
 394 the dormant season nighttime were actually greater than those for the longer P_{\max} ,



395 primarily due to diurnal variations in the daily dynamics of F_s . Overall, the influence of
 396 P_{max} on F_s uncertainty decreased with increasing $[CO_2]$ averaging time windows. This
 397 suggested that averaging $[CO_2]$ reduced the effect of gusts on the random uncertainty
 398 in estimating F_s , but led to a systematic underestimation of F_s .

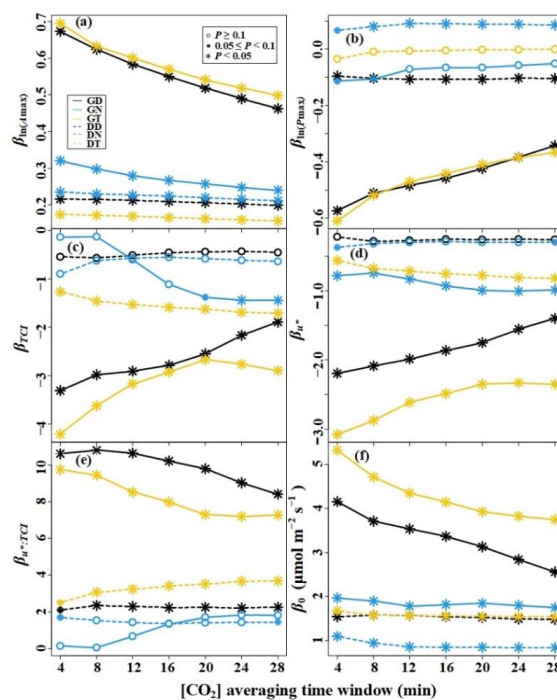


399
 400 Fig. 9 Seasonal and diurnal differences in the slope of CO_2 storage flux (F_s) versus the $F_{s,28}$ for the
 401 different CO_2 concentration ($[CO_2]$) averaging time windows. GST indicates the growing season
 402 and does not distinguish the period of maximum amplitude (P_{max}) cases, GSS indicates the
 403 growing season and a short P_{max} , GSL indicates the growing season and a long P_{max} , DST
 404 indicates the dormant season and does not distinguish P_{max} , DSS indicates the dormant season and
 405 a short P_{max} , and DSL indicates the dormant season and a long P_{max} .

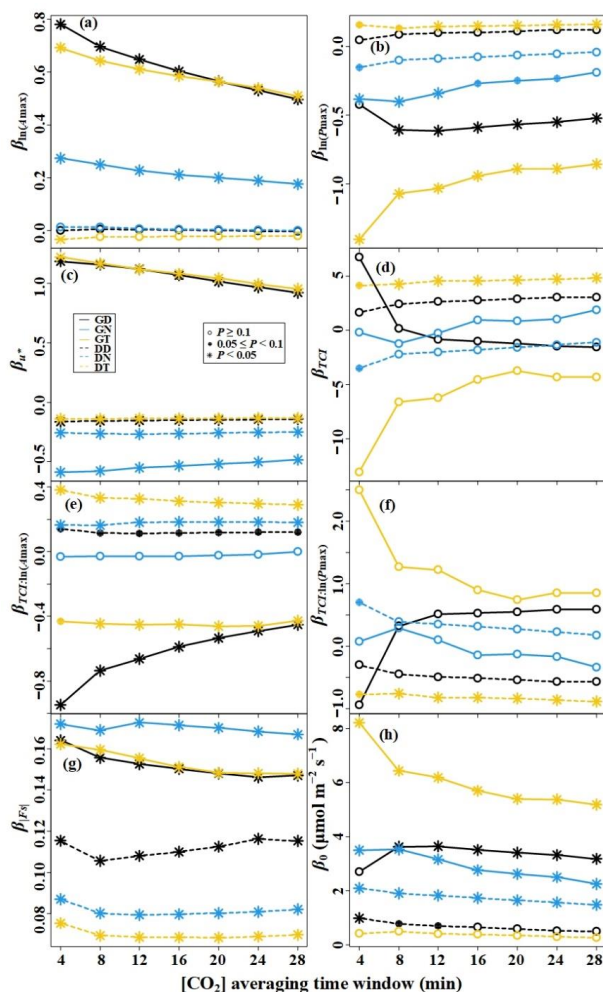
406 To analyze the effect of $[CO_2]$ fluctuations on $|F_s|$ in complex terrains, this study
 407 developed a multiple linear regression model, considering the interaction effects of
 408 wind speed and terrain complexity on $|F_s|$, as shown in Fig. 10. A_{max} exhibited a



409 significant positive correlation with $|F_s|$ in all time periods ($P < 0.05$). Conversely, P_{max}
 410 showed a significant negative correlation with $|F_s|$ during the dormant season daytime,
 411 the growing season daytime, and the transition periods ($P < 0.05$). Additionally, their
 412 correlation coefficient decreased with increasing τ . In Fig. 10d and Fig. 10e, a u^*
 413 threshold was observed during the growing season nighttime. When the u^* was below
 414 the threshold, higher TCI values resulted in smaller $|F_s|$; whereas when the u^* was above
 415 the threshold, higher TCI values led to larger $|F_s|$. During the growing season nighttime
 416 and transition periods, u^* showed a significant negative correlation ($P < 0.05$) with $|F_s|$,
 417 and the correlation coefficient decreased with increasing TCI values.



418
 419 Fig. 10 Linear regression coefficients of the CO_2 storage flux (F_s) magnitude—driving factors
 420 relationships for the seven CO_2 concentration ($[CO_2]$) averaging time windows. u^* : friction
 421 velocity; TCI: terrain complexity index; A_{max} : maximum amplitude of $[CO_2]$ fluctuations; P_{max} :
 422 corresponding period of maximum amplitude.



423

424 Fig. 11 Linear regression coefficients of the standard deviation of CO_2 storage flux (F_s)—driving
 425 factors relationships determined with Eq. (11) for the seven CO_2 concentration ($[\text{CO}_2]$) averaging
 426 time windows. u^* : friction velocity; TCI: terrain complexity index; A_{\max} : maximum amplitude of
 427 $[\text{CO}_2]$ fluctuations; P_{\max} : corresponding period of maximum amplitude.

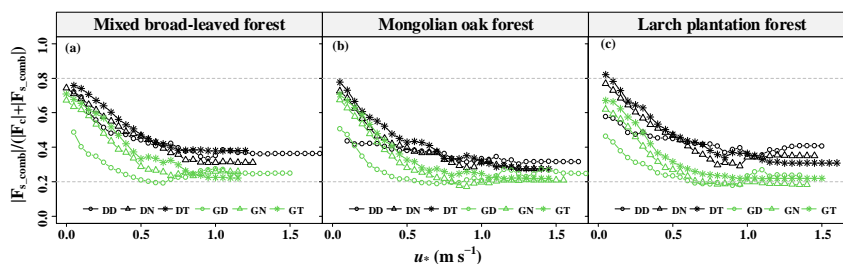
428 As evident from Fig. 11a and Fig. 11e, the A_{\max} exhibited a significant positive
 429 correlation ($P < 0.05$) with $\sigma(\varepsilon_s)$ during both the dormant season’s nighttime and the
 430 growing season. Throughout the transition period of the growing season, P_{\max} displayed
 431 a significant negative correlation with $\sigma(\varepsilon_s)$ ($P < 0.05$). During the transition period
 432 of the dormant season, a TCI threshold was observed, with P_{\max} showing a significant



433 positive correlation ($P < 0.05$) with $\sigma(\varepsilon_s)$ when the TCI was below the threshold, and
434 a significantly negative correlation ($P < 0.05$) with $\sigma(\varepsilon_s)$ when the TCI exceeded the
435 threshold (Fig. 11b and Fig. 11f). The u^* showed a significantly negative correlation
436 with $\sigma(\varepsilon_s)$ during the daytime and transition periods of the growing season ($P < 0.05$),
437 while in other time periods, u^* was significantly positively correlated with $\sigma(\varepsilon_s)$ ($P <$
438 0.05). The $|F_s|$ demonstrated a significant positive correlation with $\sigma(\varepsilon_s)$ ($P < 0.05$) in
439 all time periods, with its correlation coefficient being greater during the growing season
440 than during the dormant season. These observations suggested that the effect of
441 turbulent mixing on the magnitude of F_s and its uncertainty was regulated by terrain
442 complexity.

443 3.3 Effect of CO₂ storage fluxes uncertainty on NEE observations

444 The 30-min F_{s_comb} was obtained by weighing the bias and random error of F_s using
445 different [CO₂] averaging time windows and P_{max} values. This study then focused on
446 the magnitude of F_{s_comb} in relation to the F_c magnitude and its diurnal, seasonal, and
447 site variations. To assess the significance of F_s in NEE observations, the relative
448 contribution ratio of F_{s_comb} magnitude ($|F_{s_comb}|/(|F_c|+|F_{s_comb}|)$) was employed. The
449 $|F_{s_comb}|/(|F_c|+|F_{s_comb}|)$ showed a decreasing trend to convergence with increasing u^*
450 (Fig. 12). On average, the $|F_{s_comb}|/(|F_c|+|F_{s_comb}|)$ ranged from 17.2% to 82.0%, with a
451 higher value during the dormant season compared to the growing season. This indicated
452 that as turbulence intensity increased, the contribution of F_s to the NEE in forests
453 decreased to a constant value. Nevertheless, even under strong turbulence intensity, F_s
454 still played a significant role in the NEE observations of forests in complex terrains.



455
 456 Fig. 12 Relative contribution ratio of the CO₂ storage flux magnitude ($|F_{s_comb}|/(|F_c|+|F_{s_comb}|)$)
 457 determined by decision-level fusion model as a function of the friction velocity (u_*) moving block
 458 averages from all 30-min data for the years 2020–2021. GD represents the growing season's
 459 daytime; GN represents the growing season's nighttime; GT represents the growing season's
 460 transition period; DD represents the dormant season's daytime; DN represents the dormant
 461 season's nighttime; DT represents the dormant season's transition period.

462 As indicated in Table 3, both P_{max} and TCI exhibited a significant positive
 463 correlation with $|F_{s_comb}|/(|F_c|+|F_{s_comb}|)$ ($P < 0.05$), while both A_{max} and WS showed a
 464 significant negative correlation with $|F_{s_comb}|/(|F_c|+|F_{s_comb}|)$ ($P < 0.05$). Notably,
 465 seasonal variations in correlation coefficients were observed. The correlation between
 466 the WS and $|F_{s_comb}|/(|F_c|+|F_{s_comb}|)$ was more pronounced during both the dormant
 467 season's transition period and the growing season, and it decreased with increasing TCI
 468 values during the dormant season's daytime and nighttime.

469 Table 4 presented a comprehensive comparison of diurnal, seasonal, and site
 470 differences in slope (with intercept terms forced to zero) and NRMSE between F_{s_comb}
 471 and F_{s_28} . The slopes for the three forest stands ranged from 28.6% to 33.3%, with
 472 higher slopes observed during the growing season compared to the dormant season.
 473 This suggested that the F_{s_28} was underestimated by 28.6%–33.3% compared to the
 474 F_{s_comb} . The NRMSE of F_{s_comb} versus the F_{s_28} in the three forest stands ranged from
 475 59.2% to 67.2%.



476 Table 3 Linear regression coefficients of the relative contribution ratio of F_{s_comb}
 477 magnitudes to NEE observations ($(|F_{s_comb}|/(|F_c|+|F_{s_comb}|))$) —driving factors
 478 relationships for the six time periods.

Time period	β_0	$\ln(P_{max})^7$	$\ln(A_{max})^8$	$u^*{}^9$	TCI ¹⁰	$u^*:TCI$	R^2
Total	0.292 ***	0.048 ***	-0.037 ***	-0.334 ***	0.790 ***	-1.018 ***	0.278 ***
GD ¹	0.299 ***	0.016	-0.041 ***	-0.183 ***	-0.293 *	0.239	0.158 ***
GN ²	0.370 ***	0.029	-0.023 ***	-0.386 ***	-0.038	0.081	0.103 ***
GT ³	0.161	0.060 ***	-0.014 ***	-0.182	1.056 ***	-1.754	0.186 ***
DD ⁴	0.393 ***	0.011	-0.020 ***	-0.154 *	0.306	-0.153	0.040 ***
DN ⁵	0.661 ***	0.012	-0.026 ***	-0.443 ***	-0.035	0.399	0.088 ***
DT ⁶	0.495 ***	0.017	-0.036 ***	-0.294 ***	0.564	-0.852	0.149 ***

479 ¹ GD represents the growing season's daytime; ² GN represents the growing season's nighttime;
 480 ³ GT represents the growing season's transition period; ⁴ DD represents the dormant season's
 481 daytime; ⁵ DN represents the dormant season's nighttime; ⁶ DT represents the dormant season's
 482 transition period. ⁷ A_{max} : maximum amplitude; ⁸ P_{max} : corresponding period of maximum amplitude.
 483 ⁹ u^* : friction velocity; ¹⁰ TCI: terrain complexity index; *** represents $P < 0.001$; ** represents $P <$
 484 0.01 ; * represents $P < 0.05$.

485 To evaluate the impact of F_{s_comb} on NEE_{obs} ($F_c + F_s$), we further evaluated the
 486 slope (with intercept terms forced to zero) and NRMSE of $F_c + F_{s_comb}$ compared to F_c
 487 $+ F_{s_28}$, as presented in Table 5. The slopes for the three forest stands indicated that the
 488 NEE_{obs} with F_{s_28} was underestimated by 1.9%–4.3% compared to the NEE_{obs} with
 489 F_{s_comb} , with the order $MBF > LPF > MOF$. The underestimation of NEE_{obs} was higher
 490 (6.4%–15.5%) during the growing season nighttime and transition period but much



491 lower (< 1%) during the growing season daytime. The NRMSE of NEE_{obs} with the
 492 F_{s_comb} versus the F_{s_28} in the three forest stands ranged from 16.0% to 25.4%. The
 493 analysis suggested that combining the F_s values based on different averaging [CO_2]
 494 time windows in the decision-level fusion model could successfully weigh potential
 495 underestimation bias and random uncertainties.

496 Table 4 Statistical inference of major axis regression for the F_{s_28} calculated by
 497 combining multiple [CO_2] averaging time windows F_{s_comb} and the 28-min averaging
 498 window-based F_s

Forest	Time period	N	R^2	Slope	95% CI		NRMSE %
MBF ⁷	Total	28061	0.729	1.333	1.323	1.342	67.2
	GD ¹	5726	0.813	1.248	1.234	1.262	55.1
	GN ²	3640	0.643	1.535	1.503	1.567	85.8
	GT ³	3092	0.725	1.311	1.287	1.337	67.2
	DD ⁴	4906	0.914	1.064	1.054	1.075	32.9
	DN ⁵	6791	0.900	1.099	1.089	1.109	35.0
	DT ⁶	3906	0.948	1.068	1.059	1.077	25.0
MOF ⁸	Total	28817	0.783	1.286	1.279	1.294	59.2
	GD	5886	0.781	1.281	1.266	1.296	61.0
	GN	3799	0.752	1.338	1.318	1.358	65.6
	GT	3190	0.751	1.350	1.327	1.373	66.8
	DD	5236	0.931	1.108	1.098	1.118	31.1
	DN	6669	0.934	1.110	1.103	1.118	29.3
	DT	4037	0.951	1.079	1.070	1.088	24.7
LPF ⁹	Total	24273	0.763	1.287	1.278	1.296	61.4
	GD	4659	0.732	1.335	1.314	1.357	68.2
	GN	2995	0.733	1.444	1.418	1.472	73.7
	GT	2544	0.737	1.250	1.225	1.28	63.1
	DD	4231	0.937	1.104	1.094	1.113	29.3
	DN	6288	0.952	1.094	1.088	1.100	24.8
	DT	3556	0.963	1.071	1.064	1.079	21.2



499 ¹ GD represents the growing season's daytime; ² GN represents the growing season's nighttime;
 500 ³ GT represents the growing season's transition period; ⁴ DD represents the dormant season's
 501 daytime; ⁵ DN represents the dormant season's nighttime; ⁶ DT represents the dormant season's
 502 transition period. ⁷ MBF represents mixed broad-leaved forest; ⁸ MOF represents Mongolian oak
 503 forest; ⁹ LPF represents Larch plantation forest.

504 Table 5 Statistical inference of major axis regression for the $F_c+F_{s,28}$ (NEE_{obs})
 505 calculated by combining multiple $[CO_2]$ averaging time windows ($F_c+F_{s,comb}$) and the
 506 28-min averaging window-based NEE_{obs}

Forest	Time period	N	R^2	Slope	95% CI		NRMSE %
MBF ⁷	Total	28061	0.942	1.043	1.040	1.046	25.4
	GD ¹	5726	0.986	1.010	1.007	1.014	15.9
	GN ²	3640	0.828	1.155	1.138	1.172	50.8
	GT ³	3092	0.839	1.136	1.119	1.154	46.3
	DD ⁴	4906	0.984	1.010	1.007	1.014	12.8
	DN ⁵	6791	0.949	1.040	1.034	1.045	23.9
	DT ⁶	3906	0.949	1.050	1.043	1.058	23.9
MOF ⁸	Total	28817	0.976	1.019	1.017	1.020	16.0
	GD	5886	0.993	1.005	1.002	1.007	11.7
	GN	3799	0.908	1.078	1.067	1.089	39.1
	GT	3190	0.892	1.097	1.084	1.110	38.3
	DD	5236	0.993	1.010	1.008	1.012	8.6
	DN	6669	0.974	1.033	1.029	1.037	17.1
	DT	4037	0.972	1.022	1.016	1.027	17.7
LPF ⁹	Total	24273	0.969	1.024	1.021	1.026	18.1
	GD	4659	0.984	1.012	1.008	1.016	17.0
	GN	2995	0.938	1.062	1.052	1.072	31.9
	GT	2544	0.891	1.064	1.050	1.079	38.1
	DD	4231	0.989	1.017	1.014	1.020	10.9
	DN	6288	0.979	1.035	1.031	1.038	15.5
	DT	3556	0.980	1.030	1.025	1.035	14.8

507 ¹ GD represents the growing season daytime; ² GN represents the growing season nighttime; ³
 508 GT represents the growing season transition period; ⁴ DD represents the dormant season daytime; ⁵
 509 DN represents the dormant season nighttime; ⁶ DT represents the dormant season transition period.



510 ⁷ MBF represents mixed broad-leaved forest; ⁸ MOF represents Mongolian oak forest; ⁹ LPF
511 represents Larch plantation forest.

512 **4 Discussion**

513 4.1 Short-term [CO₂] fluctuations above the forest canopy and F_s estimates in complex
514 terrains

515 This study found that short-term fluctuations of [CO₂] above the canopy exhibited
516 a range of 1 to 10 min (Fig. 2). These fluctuations were characterized by an average
517 P_{\max} ranging from 2.313 to 2.784 min (Table 2). Our results are in line with previous
518 research using wavelet analysis, which reported fluctuation periods of [CO₂] within and
519 above the forest canopy to be between 14 and 116 s (Cava et al., 2004). Their
520 observations of the canopy waves during periods of extreme atmospheric stability
521 (when $z/L \gg 1$) exhibited a dominant period of 1–2 min, consistent with our findings.
522 The period of [CO₂] fluctuations was found to be predominantly influenced by turbulent
523 fluxes and the residence time of CO₂ within the canopy. This indicated a potential
524 correlation between P_{\max} and the residence time of CO₂ within the canopy. Fuentes et
525 al. (2006) employed a Lagrangian model and calculated the residence time of air parcels
526 released near the ground and canopy, finding values ranging from 3 to 10 min and from
527 1 to 10 min, respectively. Similarly, Edburg et al. (2011) used the standard deviation of
528 [CO₂] averages to determine CO₂ residence time at different locations, including the
529 ground, within the canopy, and in their gas mixtures, yielding values of 8.6, 3.6, and
530 5.6 min, respectively. The results of these simulation experiments are obtained from our
531 study, further supporting the association between [CO₂] fluctuations above the forest



532 canopy and CO₂ residence time.

533 Tree density and canopy structure also play a role in influencing the air parcel
534 residence time; in flat terrains, the air parcel residence time correlate with u^* (Gerken
535 et al., 2017), and an increase in vegetation leaf area leads to longer residence times
536 when turbulence is not fully penetrative. During the growing season, forests exhibit
537 higher leaf area index and canopy densities compared to the dormant season, resulting
538 in longer P_{\max} of short-term [CO₂] fluctuations above the canopy (Fig. 3). Additionally,
539 at night, stable atmospheric conditions lead to longer residence times due to suppressed
540 turbulent mixing, resulting in relatively long nighttime P_{\max} values compared to
541 daytime and transition periods (Fig. 3).

542 Complex terrains introduce multiple factors that influence [CO₂] fluctuations,
543 including gravity-induced waves, drainage, and advection. These contribute to
544 uncertainties in estimating F_s . During nighttime, long-wave radiation emitted from the
545 valley soil surface leads to the cooling and downslope acceleration of air near the soil
546 surface due to gravity, potentially causing katabatic flow. As inertia-driven upslope
547 winds are halted by katabatic acceleration, a local shallow drainage flow is established,
548 reaching a quasi-equilibrium state approximately 1.5 h after sunset (Nadeau et al., 2013).
549 Under stable atmospheric conditions, even gentle slopes (around 1°) can generate
550 strong gravity-driven waves (Belušić and Mahrt, 2012). Consequently, advection may
551 complicate the interpretation of nighttime EC measurements at certain relatively gentle
552 sites, but this complexity is not evident during daytime measurements (Leuning et al.,
553 2008). Advection plays a role in depleting the CO₂ accumulated within the canopy,



554 resulting in lower F_s fluxes and establishing an inverse relationship between storage
555 and advection (Van Gorsel et al., 2011). The occurrence of larger F_s values for long P_{\max}
556 values suggests weaker advection compared to short P_{\max} values (Fig. 4). In our study,
557 we observed that the F_s magnitude was relatively large during nighttime and transition
558 periods, while it was smaller during daytime (Fig. 4), which is consistent with the
559 findings reported by Wang et al. (2016).

560 During nighttime and transition periods in a closed canopy, the turbulent coupling
561 state above and below the canopy gradually decouples, eventually reaching complete
562 decoupling as the u^* decreases (Fig. 5). However, this decoupling does not lead to stable
563 stratification within the canopy. Despite the occurrence of decoupling and advection in
564 the closed canopy, waves are unlikely to exist within the canopy itself (Van Gorsel et
565 al., 2011). As a result, a consistent trend in the variation of F_s with τ is observed across
566 the three forest stands during the growing season, independent of P_{\max} (Fig. 9).
567 Conversely, in an open canopy where waves are present, the observations of F_s become
568 more complex. This complexity could be the primary reason why the variation of F_s
569 with $[\text{CO}_2]$ averaging time windows differs between the three forest stands for short
570 P_{\max} values during the dormant season daytime (Fig. 9). The presence of waves
571 introduces additional variability in the measurements, leading to differences in F_s
572 estimates based on different $[\text{CO}_2]$ averaging time windows in these particular
573 conditions.

574 4.2 Uncertainty in forest ecosystem F_s measurement in complex terrains

575 Previous studies have highlighted the significant the random uncertainty of F_s in



576 an open-canopy forest approximately $0.9 \mu\text{mol m}^{-2} \text{s}^{-1}$, compared to the measured
577 change in F_s of $0.3 \mu\text{mol m}^{-2} \text{s}^{-1}$ and the estimated NEE of $6.0 \mu\text{mol m}^{-2} \text{s}^{-1}$ (Van Gorsel
578 et al., 2009). In the current study, we found that the uncertainty of F_s estimates was
579 close to $2 \mu\text{mol m}^{-2} \text{s}^{-1}$ and $1 \mu\text{mol m}^{-2} \text{s}^{-1}$ for the growing and dormant seasons,
580 respectively, as F_s approached zero (Fig. 7). The result for the dormant season was
581 consistent with the previous findings. However, the estimation method employed in our
582 study, comparing observations at two similar moments and ambient conditions, is
583 susceptible to environment changes and flux footprint variability, potentially leading to
584 an overestimation of the total random uncertainty in F_s .

585 The random uncertainty of F_s shares similarities with NEE estimation. For
586 example, the magnitude of F_s measurements is positively correlated with the standard
587 deviation of random uncertainty in F_s . Additionally, the overall distribution of F_s
588 measurements exhibits a non-Gaussian distribution with a high peak, aligning with the
589 statistical properties of NEE uncertainty (Richardson et al., 2006; Richardson et al.,
590 2008). Various factors contribute to the uncertainty in F_s estimates, including flux
591 measurement footprint variations, sampling frequency, spatial sampling resolution of
592 $\text{CO}_2/\text{H}_2\text{O}$ concentrations, and instrumental measurement accuracy. The uncertainty
593 arising from variations in the flux measurement footprint is considerable, typically on
594 the order of tens of percentages, which is an order of magnitude higher than typical
595 sensor errors (Metzger, 2018). The AP200 atmospheric profiling system used in this
596 study has an accuracy of $\pm 0.5 \mu\text{mol mol}^{-1}$ and $\pm 0.1 \text{mmol mol}^{-1}$ for CO_2 and H_2O
597 concentration measurements, respectively (Montagnani et al., 2018). Efforts to reduce



598 random errors in $[\text{CO}_2]$ originating from pressure fluctuations include adding buffer
599 volumes before IRGA pumping tests (Marcolla et al., 2014). The AP200 adopts buffer
600 volumes that are fully mixed during gas extraction and performs a weighted average of
601 $[\text{CO}_2]$ instantaneous measurements to minimize the sampling error for each level's
602 $[\text{CO}_2]$ measurement (Cescatti et al., 2016).

603 The F_s estimates can be influenced by singular eddies that penetrate inside the
604 canopy (Finnigan, 2006). Accurate calculation of F_s requires considering the period of
605 $[\text{CO}_2]$ fluctuations with the eddy coherence structure. The spectral energy of the F_s time
606 series is primarily concentrated between 0.001 and 0.2 Hz (500 and 5 s, respectively).
607 However, even with sampling frequencies of 2 Hz and below, significantly lower F_s
608 values are obtained (Bjorkegren et al., 2015). The Nyquist-Shannon sampling theorem
609 dictates that accurate measurements of $[\text{CO}_2]$ require a sampling period no longer than
610 half the period of $[\text{CO}_2]$ fluctuations. Consequently, to monitor short-term changes in
611 $[\text{CO}_2]$, measurements must be taken over a period no longer than half of the period
612 corresponding to the maximum amplitude (or major energy) of $[\text{CO}_2]$ fluctuations. In
613 this study, the average P_{\max} for $[\text{CO}_2]$ fluctuations fell within the range of 2.313–2.784
614 min (Table 2). Therefore, it is crucial to ensure that the sampling period for $[\text{CO}_2]$ does
615 not exceed 1.256 to 1.392 min, which corresponds to half the average P_{\max} range.
616 Monitoring fluctuations of P_{\max} for less than 4 min during a 2-min monitoring period
617 of $[\text{CO}_2]$ presents a significant challenge. This is a primary reason that the systematic
618 bias and random error in F_s estimate with a single profile system are irreconcilable
619 (Wang et al., 2016). Short-term $[\text{CO}_2]$ fluctuations are mainly influenced by boundary



620 layer turbulence, and sampling errors in incomplete fluctuation cycles will be
621 superimposed with the real advection flux (anisotropy) dispersion in complex terrains
622 (Van Gorsel et al., 2011). This substantially increases the random uncertainty in F_s
623 based on shorter $[\text{CO}_2]$ averaging time windows (Fig. 6 and Fig. 8). As a result, the
624 deviation of NEE estimates from the actual value expands.

625 In complex terrains, the bidirectional airflow within forests along slopes can cause
626 the decoupling of soil CO_2 fluxes from EC measurements above the forest canopy
627 (Feigenwinter et al., 2008; Aubinet et al., 2003), leading to significant errors in CO_2
628 flux measurements. Forest soil serves as the primary source of CO_2 gas and regions of
629 high flux over complex terrains act like chimneys, transporting air parcels from the soil
630 surface within forests (Chen et al., 2019). In situations where turbulence is not well-
631 developed, and CO_2 mixing is inadequate, the trend of F_s with turbulence intensity
632 aligns with that of advective fluxes, which is opposite to that of turbulent fluxes
633 (Mchugh et al., 2017). The temporal dynamics and amplitudes of F_s changes are
634 influenced by topography complexity and wind conditions above the forest canopy (Fig.
635 10). Locations with more complex and sloping topography at the flux tower are more
636 likely to generate advective fluxes that may not be easily observed at a single point.

637 Estimating landscape CO_2 fluxes in complex terrains solely based on
638 measurements from a single flux tower can introduce significant errors and biases that
639 are not acceptable. The magnitude of these errors in F_s estimates is dependent on the
640 height of the forest canopy and the endogenous source/sink (Chen et al., 2020). To
641 mitigate errors and biases associated with estimating F_s in complex terrains, we



642 employed a regression modeling approach using the decision-level fusion model. This
643 method involves computing a weighted average of F_s based on different $[CO_2]$
644 averaging time windows, effectively reducing errors and biases in the estimation of F_s
645 (see Table 5). In fact, from the definition of storage flux, it can be seen that weighting
646 the storage flux is essentially weighting the $[CO_2]$ in the average time window, which
647 means replacing spatial sequences with temporal sequences for weighting. The
648 weighting coefficients used to construct the model were based on the relative errors and
649 biases of F_s estimation, with the weighting coefficient decreasing as the represented
650 moment's length increased. To obtain more accurate estimates of forest ecosystem F_s in
651 complex terrains, further research should focus on understanding the spatiotemporal
652 patterns and dynamics of $[CO_2]$.

653 **5 Conclusions**

654 This study investigated the impact of short-term $[CO_2]$ fluctuations on the
655 estimation of F_s in temperate forest ecosystems within complex terrains. Additionally,
656 it examined the F_s uncertainty and the contribution of the F_s to NEE using data from
657 three flux towers. To enhance F_s uncertainty estimation, statistical sampling techniques
658 were applied based on the individual tower approach.

659 The results highlighted the significance of considering multiple time windows for
660 averaging $[CO_2]$ when estimating F_s , as $[CO_2]$ above the forest canopies exhibited
661 fluctuations with periods ranging from 1 to 10 minutes. Diurnal, seasonal, and spatial
662 variations were observed in the amplitude and periodicity of $[CO_2]$ fluctuations,



663 highlighting the need for thoughtful sampling strategies. The use of individual gas
664 analyzers to sample the CO₂ in the control volume was inadequate, leading to
665 systematic biases and random errors in the F_s estimates. Increasing [CO₂] averaging
666 time windows mitigated the effect of [CO₂] fluctuations on F_s estimates, reducing both
667 magnitude and uncertainty.

668 The study also revealed that the uncertainty of F_s followed a non-normal
669 distribution, with its standard deviation positively correlated with F_s magnitude, which
670 has important implications for quality control. To improve F_s estimation, a decision-
671 level fusion model was introduced, integrating F_s estimates from multiple [CO₂]
672 averaging time windows, effectively reducing the impact of short-term [CO₂]
673 fluctuations while considering underestimation bias and random errors. The
674 contribution of F_s to NEE exhibited diurnal, seasonal, and spatial variations associated
675 with u^* , contributing to the NEE observations at rates ranging from 17.2% to 82.0%
676 depending on the turbulent mixing and terrain complexity. The influence of terrain
677 complexity on the relationship between [CO₂] fluctuations, turbulent mixing, and the
678 contribution of F_s to NEE was also evident. The findings from the three flux towers
679 allowed for the generalization of these results beyond the study site. These insights
680 provide crucial scientific support for the practical application of the eddy covariance
681 technique and advance our understanding of accurately estimating NEE in forest
682 ecosystems in complex terrains.

683

684 **Appendix A**



685 *A.1 the weight parameters of the decision-level fusion model*

686 For each 30-min CO₂ storage flux (F_s) estimate based on the CO₂ concentration
687 ([CO₂]) averaging time window (τ), the weight in the decision-level fusion model can
688 be obtained by weighting the random uncertainty and bias of F_{s_τ}.

689 The weight of the random uncertainty for the F_{s_τ} is expressed as follows:

$$w_{\tau} = \frac{1/\sigma(\varepsilon_{\tau})}{\sum_j 1/\sigma(\varepsilon_{\tau})}, \quad (\text{A.1})$$

690 where $\sigma(\varepsilon_{\tau})$ is the random uncertainty of the F_{s_τ}, qualified as the standard deviation.

691 The weight of the bias for the F_{s_τ} is expressed as follows:

$$W_{\tau} = \frac{K_{\tau}}{\sum_j K_j}, \quad (\text{A.2})$$

692 where K_{τ} is the slope between the F_{s_τ} and F_{s_28}.

693 Ultimately, the weight of the F_{s_τ} in the decision-level fusion model can be
694 calculated using the following equation:

$$w_{\tau}^* = rw_{\tau} + (1 - r)W_{\tau}, \quad (\text{A.3})$$

695 where r represents the proportion of the weight of random uncertainty.

696 *A.2 Complex terrain index*

697 This study employed a novel descriptor called the terrain complexity index (*TCI*)
698 to quantify the complexity of the three-dimensional terrain. For a given unit area, the
699 *TCI* equation can be expressed as follows:

$$TCI = (1 - P_d \cos \alpha)(1 - Z_d^{-1})(D_f - 2)^{H/\ln(12)}, \quad (\text{A.4})$$

700 where, P_d represented the volume of terrain above the lowest elevation of an area unit
701 (V_u) divided by the product of its largest vertically projected area (S_v) and the edge



702 length of the side of the area unit (d), expressed as $P_d = V_u/(S_v d)$; P_d was defined to
703 be one when the S_v is zero. α_d indicated the slope of the area unit. Z_d denoted the
704 terrain roughness, which defined as the ratio of the terrain surface area to the projected
705 horizontal plane. D_f is the fractal dimension of terrain surface area, which ranged from
706 2 to 3 and described the complexity in spatially self-similar structure of the local surface
707 within the area unit and the area unit surface (B. B. Mandelbrot, 1967; Taud and Parrot,
708 2005). Employing terrain surface area, the box-counting method is used to estimate
709 fractal dimension of unit area. H denoted the Shannon-Wiener index and expressed as
710 $H = -\sum_{i=1}^n P_i \ln(P_i)$, capturing the uniformity of the spatial distribution of the pixel
711 aspects within the area unit. When the aspect of each pixel was divided into 30°
712 segments, P_i denoted the proportion of the i^{th} type of pixel aspects within the area unit
713 and n was the total number of pixel aspect types within the area unit.

714 To quantify the terrain complexity of the underlying surface around the flux towers,
715 we computed the quartiles of TCI for all area units within a sector (divided by 30°) with
716 a radius of 380 m. A weighted geometric mean was employed to construct $TCIs$, which
717 describe the statistical distribution of TCI of the sector. The $TCIs$ represents the
718 topographic complexity of the sector and are calculated using the following equation:

$$719 \quad TCI_s = (TCI_5 TCI_{25} TCI_{50} TCI_{75} TCI_{95})^{1/5} \quad (\text{A.5})$$

720 where TCI_5 , TCI_{25} , TCI_{50} , TCI_{75} , and TCI_{95} are the quartiles of 5%, 25%, 50%, 75%,
721 and 95%, respectively. The $TCIs$ values range from 0 to 1, with higher values indicating
722 greater terrain complexity.

723 *Data availability.* Data used in this paper are available at the Science Data Bank



724 (<https://www.scidb.cn/en/s/7ZfQZv>) or upon request to the corresponding author.

725 *Author contributions.* DT developed the manuscript; JZ was responsible for
726 conceptualizing the idea and designing the research study; TG substantially structured
727 the manuscript; FY contributed to the data collection process; YZ helped in the design
728 and preparation of the figures and tables; XZ and BY revised the manuscript.

729 *Competing interests.* The authors declare that they have no known competing
730 financial interests or personal relationships that could have appeared to influence the
731 work reported in this paper.

732 *Acknowledgments.* We are grateful to Qingyuan Forest CERN, Chinese Academy of
733 Sciences/Qingyuan Forest, National Observation and Research Station, Liaoning
734 Province, China for providing forest sites, instrument systems, and logistic supports.

735 *Financial support.* This research was financially supported by the National Natural
736 Science Foundation of China (No. 32192435), the China Postdoctoral Science
737 Foundation (No. 2023M733672), and the Postdoctoral Research Startup Foundation
738 of Liaoning Province of China (No. 2022-BS-022).

739 **Reference**

- 740 Aubinet, M., Heinesch, B., and Yernaux, M.: Horizontal and Vertical CO₂ Advection In A Sloping Forest,
741 *Boundary-Layer Meteorology*, 108, 397-417, 10.1023/a:1024168428135, 2003.
- 742 Aubinet, M., Grelle, A., Ibrom, A., Rannik, Ü., Moncrieff, J., Foken, T., Kowalski, A. S., Martin, P. H.,
743 Berbigier, P., Bernhofer, C., Clement, R., Elbers, J., Granier, A., Grünwald, T., Morgenstern, K.,
744 Pilegaard, K., Rebmann, C., Snijders, W., Valentini, R., and Vesala, T.: Estimates of the Annual Net
745 Carbon and Water Exchange of Forests: The EUROFLUX Methodology, in: *Advances in Ecological
746 Research Volume 30, Advances in Ecological Research*, 113-175, 10.1016/s0065-2504(08)60018-5,
747 2000.
- 748 B. B. Mandelbrot: How Long Is the Coast of Britain? Statistical Self-Similarity and Fractional Dimension,
749 *Science*, 156, 636-638, 1967.
- 750 Belušić, D. and Mahrt, L.: Is geometry more universal than physics in atmospheric boundary layer flow?,
751 *Journal of Geophysical Research: Atmospheres*, 117, n/a-n/a, 10.1029/2011jd016987, 2012.



- 752 Björkegren, A. B., Grimmond, C. S. B., Kotthaus, S., and Malamud, B. D.: CO₂ emission estimation in
753 the urban environment: Measurement of the CO₂ storage term, *Atmospheric Environment*, 122, 775-790,
754 10.1016/j.atmosenv.2015.10.012, 2015.
- 755 Cava, D., Giostra, U., Siqueira, M., and Katul, G.: Organised motion and radiative perturbations in the
756 nocturnal canopy sublayer above an even-aged pine forest, *Boundary-Layer Meteorology*, 112, 129-157,
757 DOI 10.1023/B:BOUN.0000020160.28184.a0, 2004.
- 758 Cescatti, A., Marcolla, B., Goded, I., and Gruening, C.: Optimal use of buffer volumes for the
759 measurement of atmospheric gas concentration in multi-point systems, *Atmospheric Measurement*
760 *Techniques*, 9, 4665-4672, 10.5194/amt-9-4665-2016, 2016.
- 761 Chen, B., Chamecki, M., and Katul, G. G.: Effects of topography on in-canopy transport of gases emitted
762 within dense forests, *Quarterly Journal of the Royal Meteorological Society*, 145, 2101-2114,
763 10.1002/qj.3546, 2019.
- 764 Chen, B. C., Chamecki, M., and Katul, G. G.: Effects of Gentle Topography on Forest-Atmosphere Gas
765 Exchanges and Implications for Eddy-Covariance Measurements, *J Geophys Res-Atmos*, 125, ARTN
766 e2020JD032581
767 10.1029/2020JD032581, 2020.
- 768 de Araújo, A. C., J.P.H.B., O., Dolman, A. J., B., K., M.J., W., and J.R., E.: Implications of CO₂ pooling
769 on delta C13 of ecosystem respiration and leaves in Amazonian forest, *Biogeosciences*, 5, 779-795,
770 10.5194/bg-5-779-2008, 2008.
- 771 de Araújo, A. C., Dolman, A. J., Waterloo, M. J., Gash, J. H. C., Kruijt, B., Zanchi, F. B., de Lange, J. M.
772 E., Stoevelaar, R., Manzi, A. O., Nobre, A. D., Lootens, R. N., and Backer, J.: The spatial variability of
773 CO₂ storage and the interpretation of eddy covariance fluxes in central Amazonia, *Agricultural and Forest*
774 *Meteorology*, 150, 226-237, 10.1016/j.agrformet.2009.11.005, 2010.
- 775 Edburg, S. L., Stock, D., Lamb, B. K., and Patton, E. G.: The Effect of the Vertical Source Distribution
776 on Scalar Statistics within and above a Forest Canopy, *Boundary-Layer Meteorology*, 142, 365-382,
777 10.1007/s10546-011-9686-1, 2011.
- 778 Feigenwinter, C., Bernhofer, C., and Vogt, R.: The Influence of Advection on the Short Term CO₂-Budget
779 in and Above a Forest Canopy, *Boundary-Layer Meteorology*, 113, 201-224,
780 10.1023/B:BOUN.0000039372.86053.ff, 2004.
- 781 Feigenwinter, C., Bernhofer, C., Eichelmann, U., Heinesch, B., Hertel, M., Janous, D., Kolle, O.,
782 Lagergren, F., Lindroth, A., Minerbi, S., Moderow, U., Mölder, M., Montagnani, L., Queck, R., Rebmann,
783 C., Vestin, P., Yernaux, M., Zeri, M., Ziegler, W., and Aubinet, M.: Comparison of horizontal and vertical
784 advective CO₂ fluxes at three forest sites, *Agricultural and Forest Meteorology*, 148, 12-24,
785 10.1016/j.agrformet.2007.08.013, 2008.
- 786 Finnigan, J.: The storage term in eddy flux calculations, *Agricultural and Forest Meteorology*, 136, 108-
787 113, 10.1016/j.agrformet.2004.12.010, 2006.
- 788 Finnigan, J., Ayotte, K., Harman, I., Katul, G., Oldroyd, H., Patton, E., Poggi, D., Ross, A., and Taylor,
789 P.: Boundary-Layer Flow Over Complex Topography, *Boundary-Layer Meteorology*, 177, 247-313,
790 10.1007/s10546-020-00564-3, 2020.
- 791 Fuentes, J. D., Wang, D., Bowling, D. R., Potosnak, M., Monson, R. K., Goliff, W. S., and Stockwell, W.
792 R.: Biogenic Hydrocarbon Chemistry within and Above a Mixed Deciduous Forest, *Journal of*
793 *Atmospheric Chemistry*, 56, 165-185, 10.1007/s10874-006-9048-4, 2006.
- 794 Gao, T., Yu, L.-Z., Yu, F.-Y., Wang, X.-C., Yang, K., Lu, D.-L., Li, X.-F., Yan, Q.-L., Sun, Y.-R., Liu, L.-
795 F., Xu, S., Zhen, X.-J., Ni, Z.-D., Zhang, J.-X., Wang, G.-F., Wei, X.-H., Zhou, X.-H., and Zhu, J.-J.:



- 796 Functions and applications of Multi-Tower Platform of Qingyuan Forest Ecosystem Research Station of
797 Chinese Academy of Sciences, *Chinese journal of applied ecology*, 31, 695-705, 10.13287/j.1001-
798 9332.202003.040, 2020.
- 799 Gerken, T., Chamecki, M., and Fuentes, J. D.: Air-Parcel Residence Times Within Forest Canopies,
800 *Boundary-Layer Meteorology*, 165, 29-54, 10.1007/s10546-017-0269-7, 2017.
- 801 Gu, L., Massman, W. J., Leuning, R., Pallardy, S. G., Meyers, T., Hanson, P. J., Riggs, J. S., Hosman, K.
802 P., and Yang, B.: The fundamental equation of eddy covariance and its application in flux measurements,
803 *Agricultural and Forest Meteorology*, 152, 135-148, 10.1016/j.agrformet.2011.09.014, 2012.
- 804 Heinesch, B., Yernaux, M., and Aubinet, M.: Some methodological questions concerning advection
805 measurements: a case study, *Boundary-Layer Meteorology*, 122, 457-478, 10.1007/s10546-006-9102-4,
806 2007.
- 807 Hollinger, D. Y. and Richardson, A. D.: Uncertainty in eddy covariance measurements and its application
808 to physiological models, *Tree Physiol*, 25, 873-885, DOI 10.1093/treephys/25.7.873, 2005.
- 809 Huang, N. E., Shen, Z., Long, S. R., Wu, M. C., Shih, H. H., Zheng, Q., Yen, N.-C., Tung, C. C., and Liu,
810 H. H.: The empirical mode decomposition and the Hilbert spectrum for nonlinear and non-stationary
811 time series analysis, *Proceedings of the Royal Society of London. Series A: Mathematical, Physical and*
812 *Engineering Sciences*, 454, 903-995, 10.1098/rspa.1998.0193, 1998.
- 813 Khélifa, N., Lecollinet, M., and Himbert, M.: Molar mass of dry air in mass metrology, *Measurement*,
814 40, 779-784, 10.1016/j.measurement.2006.05.009, 2007.
- 815 Leuning, R., Zegelin, S. J., Jones, K., Keith, H., and Hughes, D.: Measurement of horizontal and vertical
816 advection of CO₂ within a forest canopy, *Agricultural and Forest Meteorology*, 148, 1777-1797,
817 10.1016/j.agrformet.2008.06.006, 2008.
- 818 Li, S., Yan, Q., Liu, Z., Wang, X., Yu, F., Teng, D., Sun, Y., Lu, D., Zhang, J., Gao, T., and Zhu, J.:
819 Seasonality of albedo and fraction of absorbed photosynthetically active radiation in the temperate
820 secondary forest ecosystem: A comprehensive observation using Qingyuan Ker towers, *Agricultural and*
821 *Forest Meteorology*, 333, 10.1016/j.agrformet.2023.109418, 2023.
- 822 Li, Y.-C., Liu, F., Wang, C.-K., Gao, T., and Wang, X.-C.: Carbon budget estimation based on different
823 methods of CO₂ storage flux in forest ecosystems, *Chinese journal of applied ecology*, 31, 3665-3673,
824 10.13287/j.1001-9332.202011.004, 2020.
- 825 Marcolla, B., Cobbe, I., Minerbi, S., Montagnani, L., and Cescatti, A.: Methods and uncertainties in the
826 experimental assessment of horizontal advection, *Agricultural and Forest Meteorology*, 198-199, 62-71,
827 10.1016/j.agrformet.2014.08.002, 2014.
- 828 McHugh, I. D., Beringer, J., Cunningham, S. C., Baker, P. J., Cavagnaro, T. R., Mac Nally, R., and
829 Thompson, R. M.: Interactions between nocturnal turbulent flux, storage and advection at an "ideal"
830 eucalypt woodland site, *Biogeosciences*, 14, 3027-3050, 10.5194/bg-14-3027-2017, 2017.
- 831 McMaster, G. S. and Wilhelm, W. W.: Growing degree-days: one equation, two interpretations,
832 *Agricultural and Forest Meteorology*, 87, 291-300, Doi 10.1016/S0168-1923(97)00027-0, 1997.
- 833 Metzger, S.: Surface-atmosphere exchange in a box: Making the control volume a suitable representation
834 for in-situ observations, *Agricultural and Forest Meteorology*, 255, 68-80,
835 10.1016/j.agrformet.2017.08.037, 2018.
- 836 Montagnani, L., Grunwald, T., Kowalski, A., Mammarella, I., Merbold, L., Metzger, S., Sedlak, P., and
837 Siebicke, L.: Estimating the storage term in eddy covariance measurements: the ICOS methodology, *Int*
838 *Agrophys*, 32, 551-567, 10.1515/intag-2017-0037, 2018.
- 839 Montagnani, L., Manca, G., Canepa, E., Georgieva, E., Acosta, M., Feigenwinter, C., Janous, D.,



- 840 Kerschbaumer, G., Lindroth, A., Minach, L., Minerbi, S., Mölder, M., Pavelka, M., Seufert, G., Zeri, M.,
841 and Ziegler, W.: A new mass conservation approach to the study of CO₂ advection in an alpine forest,
842 *Journal of Geophysical Research*, 114, 10.1029/2008jd010650, 2009.
- 843 Nadeau, D. F., Pardyjak, E. R., Higgins, C. W., Huwald, H., and Parlange, M. B.: Flow during the evening
844 transition over steep Alpine slopes, *Quarterly Journal of the Royal Meteorological Society*, 139, 607-624,
845 10.1002/qj.1985, 2013.
- 846 Nicolini, G., Aubinet, M., Feigenwinter, C., Heinesch, B., Lindroth, A., Mamadou, O., Moderow, U.,
847 Molder, M., Montagnani, L., Rebmann, C., and Papale, D.: Impact of CO₂ storage flux sampling
848 uncertainty on net ecosystem exchange measured by eddy covariance, *Agricultural and Forest
849 Meteorology*, 248, 228-239, 10.1016/j.agrformet.2017.09.025, 2018.
- 850 Richardson, A. D., Hollinger, D. Y., Burba, G. G., Davis, K. J., Flanagan, L. B., Katul, G. G., William
851 Munger, J., Ricciuto, D. M., Stoy, P. C., Suyker, A. E., Verma, S. B., and Wofsy, S. C.: A multi-site
852 analysis of random error in tower-based measurements of carbon and energy fluxes, *Agricultural and
853 Forest Meteorology*, 136, 1-18, 10.1016/j.agrformet.2006.01.007, 2006.
- 854 Richardson, A. D., Mahecha, M. D., Falge, E., Kattge, J., Moffat, A. M., Papale, D., Reichstein, M.,
855 Stauch, V. J., Braswell, B. H., Churkina, G., Kruijt, B., and Hollinger, D. Y.: Statistical properties of
856 random CO₂ flux measurement uncertainty inferred from model residuals, *Agricultural and Forest
857 Meteorology*, 148, 38-50, 10.1016/j.agrformet.2007.09.001, 2008.
- 858 Sha, J., Zou, J., and Sun, J.: Observational study of land-atmosphere turbulent flux exchange over
859 complex underlying surfaces in urban and suburban areas, *SCIENCE CHINA-EARTH SCIENCES*, 64,
860 1050-1064, 10.1007/s11430-020-9783-2, 2021.
- 861 Siebicke, L., Steinfeld, G., and Foken, T.: CO₂-gradient measurements using a parallel multi-analyzer
862 setup, *Atmospheric Measurement Techniques*, 4, 409-423, 10.5194/amt-4-409-2011, 2011.
- 863 Taud, H. and Parrot, J.-F.: Measurement of DEM roughness using the local fractal dimension,
864 *Géomorphologie : relief, processus, environnement*, 11, 327-338, 10.4000/geomorphologie.622, 2005.
- 865 van Gorsel, E., Harman, I. N., Finnigan, J. J., and Leuning, R.: Decoupling of air flow above and in plant
866 canopies and gravity waves affect micrometeorological estimates of net scalar exchange, *Agricultural
867 and Forest Meteorology*, 151, 927-933, 10.1016/j.agrformet.2011.02.012, 2011.
- 868 van Gorsel, E., Delpierre, N., Leuning, R., Black, A., Munger, J. W., Wofsy, S., Aubinet, M., Feigenwinter,
869 C., Beringer, J., Bonal, D., Chen, B., Chen, J., Clement, R., Davis, K. J., Desai, A. R., Dragoni, D., Etzold,
870 S., Grünwald, T., Gu, L., Heinesch, B., Hutya, L. R., Jans, W. W. P., Kutsch, W., Law, B. E., Leclerc, M.
871 Y., Mammarella, I., Montagnani, L., Noormets, A., Rebmann, C., and Wharton, S.: Estimating nocturnal
872 ecosystem respiration from the vertical turbulent flux and change in storage of CO₂, *Agricultural and
873 Forest Meteorology*, 149, 1919-1930, 10.1016/j.agrformet.2009.06.020, 2009.
- 874 Wang, J., Shi, T., Yu, D., Teng, D., Ge, X., Zhang, Z., Yang, X., Wang, H., and Wu, G.: Ensemble
875 machine-learning-based framework for estimating total nitrogen concentration in water using drone-
876 borne hyperspectral imagery of emergent plants: A case study in an arid oasis, NW China, *Environmental
877 Pollution*, 266, 10.1016/j.envpol.2020.115412, 2020.
- 878 Wang, X., Wang, C., Guo, Q., and Wang, J.: Improving the CO₂ storage measurements with a single
879 profile system in a tall-dense-canopy temperate forest, *Agricultural and Forest Meteorology*, 228-229,
880 327-338, 10.1016/j.agrformet.2016.07.020, 2016.
- 881 Warton, D. I., Duursma, R. A., Falster, D. S., and Taskinen, S.: smatr 3- an R package for estimation and
882 inference about allometric lines, *Methods in Ecology and Evolution*, 3, 257-259, 10.1111/j.2041-
883 210X.2011.00153.x, 2012.



- 884 Webb, E. K., Pearman, G. I., and Leuning, R.: Correction of flux measurements for density effects due
885 to heat and water vapour transfer, *Quarterly Journal of the Royal Meteorological Society*, 106, 85-100,
886 10.1002/qj.49710644707, 1980.
- 887 Xu, K., Pingintha-Durden, N., Luo, H., Durden, D., Sturtevant, C., Desai, A. R., Florian, C., and Metzger,
888 S.: The eddy-covariance storage term in air: Consistent community resources improve flux measurement
889 reliability, *Agricultural and Forest Meteorology*, 279, 10.1016/j.agrformet.2019.107734, 2019.
- 890 Yang, B., Hanson, P. J., Riggs, J. S., Pallardy, S. G., Heuer, M., Hosman, K. P., Meyers, T. P., Wullschlegel,
891 S. D., and Gu, L.-H.: Biases of CO₂ storage in eddy flux measurements in a forest pertinent to vertical
892 configurations of a profile system and CO₂ density averaging, *Journal of Geophysical Research*, 112,
893 10.1029/2006jd008243, 2007.
- 894 Yang, P. C., Black, T. A., Neumann, H. H., Novak, M. D., and Blanken, P. D.: Spatial and temporal
895 variability of CO₂ concentration and flux in a boreal aspen forest, *J Geophys Res-Atmos*, 104, 27653-
896 27661, Doi 10.1029/1999jd900295, 1999.
- 897 Yao, Y., Zhang, Y., Yu, G., Song, Q., Tan, Z., and Zhao, J.: Estimation of CO₂ storage flux between forest
898 and atmosphere in a tropical forest, *Journal of Beijing Forestry University*, 33, 23-29, 2011.
- 899 Zhang, M., Wen, X., Yu, G.-r., Zhang, L.-m., Fu, Y., Sun, X., and Han, S.-j.: Effects of CO₂ storage flux
900 on carbon budget of forest ecosystem, *Chinese journal of applied ecology*, 21, 1201-1209, 2010.
- 901 Zhu, J., Gao, T., Yu, L., Yu, F., Yang, K., Lu, D., Yan, Q., Sun, Y., Liu, L., Xu, S., Zhang, J., Zheng, X.,
902 Song, L., and Zhou, X.: Functions and Applications of Multi-tower Platform of Qingyuan Forest
903 Ecosystem Research Station of Chinese Academy of Sciences (Qingyuan Ker Towers), *Bulletin of the*
904 *Chinese Academy of Sciences*, 36, 351-361, 10.16418/j.issn.1000-3045.20210304002, 2021.